# Supporting Information for:
# Unraveling scaling properties of slow-slip events

Luca Dal Zilio[1,2*], Nadia Lapusta[1,2], Jean-Philippe Avouac[1,2]

[1] Division of Geological and Planetary Sciences, California Institute of Technology

[2] Division of Engineering and Applied Sciences, California Institute of Technology

## Contents of this file

## Numerical methodology for simulating slow-slip events

For numerical simulations of long-term fault behavior, we use the numerical code BICyclE (Boundary Integral Cycles of Earthquakes) (Lapusta et al., 2000; Lapusta & Liu, 2009; Noda & Lapusta, 2010; Noda et al., 2013), which solves the coupled problem of elasto-dynamic equations of motion, fault friction, and off-fault diffusion of heat and pore fluids. At each fault point during slip, dynamic shear stress (or forcing) must be equal to friction (or fault shear strength). The resulting spontaneous evolution of fault slip is a complex non-linear process governed by multiple feedbacks. Shear stress at each fault point is affected by motion of all other fault points through wave-mediated dynamic and eventually static stress changes. At the same time, frictional resistance itself is coupled to slip rate and, through the state variable, to prior history of slip. Our computational approach employs an efficient boundary-integral method in the Fourier domain, which allows us to resolve the slow tectonic loading, slow-slip event nucleation and propagation — including possible radiation of seismic waves — and the afterslip transient that can follow large slip events. An adaptive time stepping is used to numerically resolve slow tectonic loading, slow-slip nucleation and propagation, and aseismic slip transients.

We consider a megathrust fault segment embedded into an elastic medium, loaded by deep-seated slip at the long term slip rate, and governed by rate-and-state friction (Dieterich, 1979; Dieterich et al., 1981; Ruina, 1983; Marone, 1998; Beeler et al., 1996, 2008):

$$\tau = f\,\overline{\sigma} = \left[ f_* + a\,ln\frac{V}{V_*} + b\,ln\frac{\theta V}{D_{RS}} \right] \overline{\sigma} \ , \tag{1}$$

$$\frac{d\theta}{dt} = 1 - \frac{V\theta}{D_{RS}} \ , \tag{2}$$

where $\tau$ is the shear resistance, $V$ is the instantaneous slip rate, $\overline{\sigma} = \sigma - p$ is the effective normal stress accounting for pore fluid pressure $p$, $f_*$ is the steady-state friction at the reference slip rate $V_*$ , $a$, $b$, and $D_{RS}$ are rate-and-state parameters, and $\theta$ is a state variable that describes the evolutionary effects in response to changing slip rates. This law, commonly referred to as the Dieterich-Ruina or aging rate-

and-state friction, has experimental support (Beeler et al., 1996) and partial theoretical justification (Rice et al., 2001). Other formulations for the evolution of the state variable exist, such as the slip law (Ruina, 1983) as well as various composite laws, and the formulation that best describes various laboratory experiments remains a topic of ongoing research (Bhattacharya et al., 2017). For a constant slip velocity $V$, the state variable $\theta$ evolves to its steady-state value $\theta_{ss} = D_{RS}/V$, transforming the shear resistance $\tau$ into its steady-state form

$$\tau_{ss} = \left[ f_* \ + (a-b) ln \frac{V}{V_*} \right] \overline{\sigma} \ , \tag{3}$$

which highlights the importance of the non-dimensional parameter $(a-b)$ of the rate dependence of friction: stable slip for velocity-strengthening (VS) friction, $(a-b)>0$, and conditionally unstable slip for velocity-weakening (VW) friction, $(a-b)<0$ (Rice & Ruina, 1983; Scholz, 1998).

Some of our models, including the reference model discussed in the main text, include the evolution of pore pressure $p$ due to inelastic shear dilatancy $\phi$ according to the following equation (Segall & Rice, 1995; Segall et al., 2010; Segall & Rice, 2006):

$$\frac{\partial p}{\partial t} = \alpha_{hy} \frac{\partial^2 p}{\partial y^2} - \frac{F(y)}{\beta} \frac{d\phi}{dt} \, , \tag{4}$$

where $\alpha_{hy}$ is the hydraulic diffusivity, $\beta$ is the specific storage, $d\phi/dt$ is the rate of change in the porosity due to inelastic deformation, and $F(y)$ is the Gaussian function representing the distribution of the inelastic porosity over the thickness of the shear zone ($W_{sz}$). Following Segall and Rice (1995), we associate the effects of dilatancy and compaction with the evolution of state variable within the fault gouge, as motivated by experiments of Marone et al. (1990), so that:

$$\delta\phi = -\epsilon \, ln \left( \frac{V_0 \, \theta}{D_{RS}} \right) , \tag{5}$$

$$\frac{d\phi}{dt} = -\epsilon \, \frac{d}{dt} \, ln \, \left( \frac{V_0 \, \theta}{D_{RS}} \right) = \frac{\epsilon}{\theta} \, \frac{d\theta}{dt}, \tag{6}$$

where $\epsilon$ is a constant derived empirically (Table S1) (Marone et al., 1990), and $D_{RS}$ is the characteristic slip. Above steady state conditions, i.e. for $\theta > D_{RS}/V$, $\theta$ decreases (gouge dilatancy), while

below steady state, $\theta$ increases (gouge compaction). With this approach, slow-slip events nucleate in areas of unstable friction under drained conditions but, as slip accelerates, dilatancy reduces pore pressure quenching instability (Segall et al., 2010).

The thrust fault between a subducting oceanic plate and overlying continental plate is modeled as a 2-D planar interface embedded in a 3-D elastic half-space. The fault extends 320 km along the strike direction and 60 km along the downdip direction. The planar fault is discretized by 1360 x 280 grid cells along the strike and downdip directions, respectively. The cell sizes are thus 250 m along strike and along downdip. A uniform tectonic loading at rate of 40 mm/yr is applied further downdip to represent the convergence rate between the Juan de Fuca and North American plates in northern Cascadia (Michel et al., 2018). We assign a velocity-weakening (VW) friction patch extending 300 km along the strike direction (length $L$) and 25 km along the downdip direction (width $W$); elsewhere, fault friction is assumed to be velocity strengthening (VS). The model setup with a narrow width is designed to favor SSEs. The effective compressive normal stress $\overline{\sigma}$ is taken to be constant at 10 MPa; this distribution of $\overline{\sigma}$ is appropriate for an over-pressurized crust at depth (Suppe, 2014; Audet et al., 2009; Leeman et al., 2016). The corresponding elevated pore fluid pressures are required by all friction models to reproduce realistic properties of slow-slip events (Shibazaki & Iio, 2003; Liu & Rice, 2005, 2007; Shibazaki & Shimamoto, 2007; Rubin, 2008; Liu & Rubin, 2010; Matsuzawa et al., 2010; Hawthorne & Rubin, 2013; D. Li & Liu, 2016; Luo & Ampuero, 2018; Viesca & Dublanchet, 2018); high pore-fluid pressures also promote slow slip in models with bulk effects (Gao & Wang, 2017). As SSEs are now found nearly universally at subduction zones (Bartlow et al., 2011; Kato & Nakagawa, 2014; Tsang et al., 2015; Fu et al., 2015; Michel et al., 2018; S. Li et al., 2016; Villegas-Lanza et al., 2016; Houston et al., 2011), such high pore fluid pressures — and the associated low effective normal stresses — may be prevalent at most subduction zones, at least at the locations of slow-slip events.

**Theoretical estimates of nucleation size and cohesive zone size**

For 2D problems with velocity-weakening rate-and-state friction and no dilatancy effects, two theoretical estimates of the earthquake nucleation size are $h^*_{rr}$ (Rice & Ruina, 1983) and $h^*_{ra}$ (Rubin & Ampuero, 2005):

$$h^*_{rr} = \frac{\pi}{4} \frac{\mu^* D_{RS}}{\overline{\sigma}\,(b-a)}; \tag{7}$$

$$h^*_{ra} = \frac{2}{\pi} \frac{\mu^* D_{RS}\, b}{\overline{\sigma}\,(b-a)^2}; \tag{8}$$

where $\mu^* = \mu$ for mode $III$, $\mu^* = \mu/(1-\nu)$ for mode II, $\mu$ is the shear modulus, $\nu$ is the Poisson's ratio, and the estimate (7) is valid for $0.5 < a/b < 1$, as explained in Rubin and Ampuero (2005). In the parameter regime $0 < a/b < 0.3781$, that study advocates $b$ instead of $(b-a)^2/b$ in the above formula; however, $(b-a)^2/b \to b$ as $a \to 0$, so that eq. 8 should approximately capture both cases. Indeed, in our exploration of parameters for the occurrence of slow-slip events, as discussed in the next section, we see no break in behavior between the two regimes of $a/b$.

In 3D problems, the nucleation size is given by Chen and Lapusta (2009):

$$h^* = (\pi^2/4) h^*_{ra}. \tag{9}$$

The theoretically estimated nucleation sizes in our models are ∼8.5–11 km based on eq. 7, and ∼29–31 km based on eq. 8. Table S1 summarizes the values of parameters used in the models. The chosen values of $D_{RS}$ are larger than those obtained in laboratory, which facilitate our numerical computation (Lapusta & Liu, 2009).

Two important physical scales in the problem are the nucleation size $h^*$ and cohesive zone size $\Lambda$. The nucleation size is a crucial length scale during interseismic periods and $h^*$ / $\Delta x$ is an important criterion to assess spatial resolution. The cohesive zone size is an important resolution criterion in dynamic rupture because it gives the spatial length scale over which the shear stress drops from its peak to residual values at the propagating rupture front (Palmer & Rice, 1973; Day et al., 2005). For

rate-and-state friction law, $\Lambda_0$, the size of $\Lambda$ at zero rupture speed $v_r$, is given as:

$$\Lambda_0 = C_1 \frac{\mu^* D_{RS}}{b\sigma} . \tag{10}$$

where $C_1$ is a constant and equal to $9\pi/32$ if the stress traction distribution within the cohesive zone is linear in space. Day et al. (2005) established that $\Lambda_0$ / $\Delta x$ of 3 to 5 is required to resolve dynamic rupture. The ratio of nucleation zone size and cohesive zone size is given by $\Lambda_0$ / $h^* \sim (b-a)^2$ / $b^2$. With the chosen values of $a$ and $b$, this ratio in our models is between 0.3 and 0.5. Therefore, resolving the cohesive zone is the more stringent numerical criterion here. In our models, we choose the cell size small enough to resolve the cohesive zone with at least 30 cells. Hence the spatial discretization in the simulations, with the cell size of $\Delta x$ = 250 m, is small enough to resolve the evolution of stress and slip rate.

The addition of dilatancy stabilizes the problem (Segall & Rice, 1995; Segall et al., 2010; Rubin, 2008; Liu & Rubin, 2010). For the parameters used (see Table S1), our SSEs nucleate in areas of unstable friction under drained conditions and hence the nucleation size estimate $h^*_{rr}$ is valid. This occurs because the off-fault diffusivity is high enough that the pore pressure inside the shearing zone equilibrates with the pore pressure outside rapidly enough for the dilatancy not to affect pore fluid pressure.

**Parameter regime for SSEs in our simulations**

We extensively explore the effect of frictional parameters on the resulting behavior of our model (Fig. S1). By increasing the characteristic slip $D_{RS}$ (from 4 to 90 mm; Table S1), our models show four different slip patterns: 1) fast (seismic) events, 2) slow-slip events, 3) decay oscillations, and 4) stable creep (Fig. S1A). We also analyze the effects of the rate-and-state properties by performing experiments with different $b-a$ (from 0.004 to 0.01; Fig. S1B), and $(b-a)/b$ (from 0.28 to 0.71), which give results in agreement with previous studies (Veedu & Barbot, 2016; Barbot, 2019). According

to our models (Fig. S1E), SSEs appear in a parameter regime between steady slip and regular (fast) earthquakes.

In particular, the conditions that lead to SSEs for rate-and-state faults with no dilatancy effect are given by:

$$\begin{cases} \frac{1}{3}W < h^*_{rr} < \frac{1}{2}W; \\ \\ h^*_{ra} > W; \end{cases} \tag{11}$$

That is, the SSEs appear when the fault width $W$ is smaller than the nucleation estimate $h^*_{ra}$ but larger, by a factor of 2 to 3, then the nucleation estimate $h^*_{rr}$. This condition makes qualitative sense given the nature of the estimates. On the one hand, $h^*_{rr}$ was obtained as the critical wavelength from a linearized quasi-static stability analysis of steady sliding to perturbations of different wavelengths, with the smaller wavelengths leading to decaying perturbations and larger wavelengths leading to growing perturbations (Rice & Ruina, 1983). Hence $h^*_{rr}$ is an estimate of the wavelengths that would result in some slip instability, explaining why the SSEs spontaneously arise when $h^*_{rr}$ is smaller than $W$. On the other hand, $h^*_{ra}$ was obtained from the energy balance of the nucleation process that takes the form of an expanding crack, giving the upper bound on the crack dimension (Rubin & Ampuero, 2005). Previous studies have shown that $h^*_{ra}$ is a good estimate of the nucleation zone at the transition from quasi-static to seismic (weave-producing) slip (Chen & Lapusta, 2009). Hence making $W$ smaller than $h^*_{ra}$ ensures that accelerating quasi-static slip does not transition into faster, seismic earthquakes.

Dilatancy effects are then explored for models M1–M4 listed in Table S2. The models show that dilatancy slows down the rupture velocity of SSEs, shifting the results towards relatively longer event durations and thus enabling a wide time spectrum ranging from a few days to several weeks and months (Ide et al., 2007).

**Measurements of SSE duration and moment release**

For each numerical experiment, we analyze all slow-slip events to determine their duration, along-strike length, area, rupture velocity, and magnitude. The events are identified using a slip-velocity threshold. With this approach, each SSE lasts while the slip velocity exceeds a threshold equal to $1.26$ x $10^{-8}$ m/s (i.e., 10 times faster than the long-term slip rate). In order to assess possible uncertainties in the duration and moment release of each event, we also include results for a standard deviation of 20% ($1.26$ x $10^{-8}$ m/s $\pm$ $2.5$ x $10^{-9}$ m/s). The sensitivity of our results to the slip-velocity threshold is tested by assuming a different definition for SSEs, with the velocity threshold which is only 2 times faster than the long-term slip rate and a minimum moment release rate of 1 x $10^{14}$ Nm/day. The resulting properties of SSEs have minimal variations (Fig. S4). The choice of the slip-velocity threshold is to ensure that (1) selected SSEs have velocities exceeding the plate convergence rate at the minimum and (2) it is around the lower resolution limit of GPS slip inversion models in order to compare modeled SSE source parameters to those inferred from geodetic observations. For SSEs in Cascadia, Michel et al. (2018) found that the minimum resolved slip rate is 0.21 mm/day (i.e., 2 times the long-term slip rate) at the lower resolution limits for their network inversion filter models, whereas Wech and Bartlow (2014) found a minimum resolved slip rate of $\sim$0.25 to 0.5 mm/day (2.2–4.5 times the long-term slip rate).

**Measurements of stress drop**

We consider the average energy-based stress drops ($\overline{\Delta\sigma_E}$) (Noda et al., 2013), which has been recently used to analyze earthquakes (Ye et al., 2016). $\overline{\Delta\sigma_E}$ corresponds to averaging the stress drop distribution $\Delta\sigma(x_1, x_3)$ the actual final slip $\Delta u$ at each point as the weighting function:

$$\overline{\Delta\sigma_E} = \frac{\int_{\sum} \Delta\sigma \, \Delta u \, dS}{\int_{\sum} \Delta u \, dS}, \tag{12}$$

where $S$ is the planar fault area, $\Delta\sigma$ is the initial shear stress minus the final shear stress at each ruptured location, $\Delta u$ is the final slip distribution produced by the event. This measure is more convenient than the more commonly used moment-based stress drop, as the moment-based stress drop requires the determination of the shape of the ruptured area and computation of the appropriate weighting function (47). Defining the ruptured area of a slow-slip event would require an additional criterion of what constitutes significant slip, which is typically defined as a percentage of the maximum slip.

| ***Parameter*** | ***Symbol*** | ***Value*** |
|---|---|---|
| Background characteristic slip distance | $D_{RS}$ | 5-90 mm |
| Rate-and-state properties in VW region | $a$ | 0.002-0.010 |
| | $b$ | 0.006-0.016 |
| Rate-and-state properties in VS region | $a$ | 0.019 |
| | $b$ | 0.014 |
| Effective normal stress | $\bar{\sigma} = \sigma_n - p$ | 10 MPa |
| Dilatancy coefficient | $\epsilon$ | 0; $3 \cdot 10^{-4}$ |
| Hydraulic diffusivity | $\alpha_{hy}$ | $1 \cdot 10^{-6}$ m$^2$/s |
| Specific storage | $\beta$ | $5 \cdot 10^{-11}$ 1/Pa |
| Thickness of the shear zone | $W_{sz}$ | $1 \cdot 10^{-3}$ m |
| Reference friction coefficient | $f_*$ | 0.6 |
| Reference slip velocity | $V_*$ | $10^{-6}$ m/s |
| Poisson's ratio | $\nu$ | 0.25 |
| Shear modulus | $\mu$ | 30 GPa |
| Loading rate | $V_{pl}$ | 40 mm/yr |
| Spatial resolution | $\Delta_x$ | 250 m |
| Width of VW region | $W$ | 25 km |
| Length of VW region | $L$ | 300 km |

**Table S1:** Model parameters used in this study.

| ***Model*** | $a$ | $b$ | $D_{RS}$ *(mm)* | Dilatancy coefficient ($\epsilon$) |
|---|---|---|---|---|
| ***M1*** | 0.004 | 0.014 | 45 | / |
| ***M1-D**** | 0.004 | 0.014 | 45 | $3 \cdot 10^{-4}$ |
| ***M2*** | 0.002 | 0.006 | 19 | / |
| ***M3*** | 0.0028 | 0.0088 | 27 | / |
| ***M4*** | 0.0032 | 0.0112 | 36 | / |

**** The reference model shown in Fig. 2–4.***

**Table S2:** Parameters of the selected models, for which the scaling is shown in Fig. S4. M1 and M1-D have the same properties other than dilatancy coefficient.

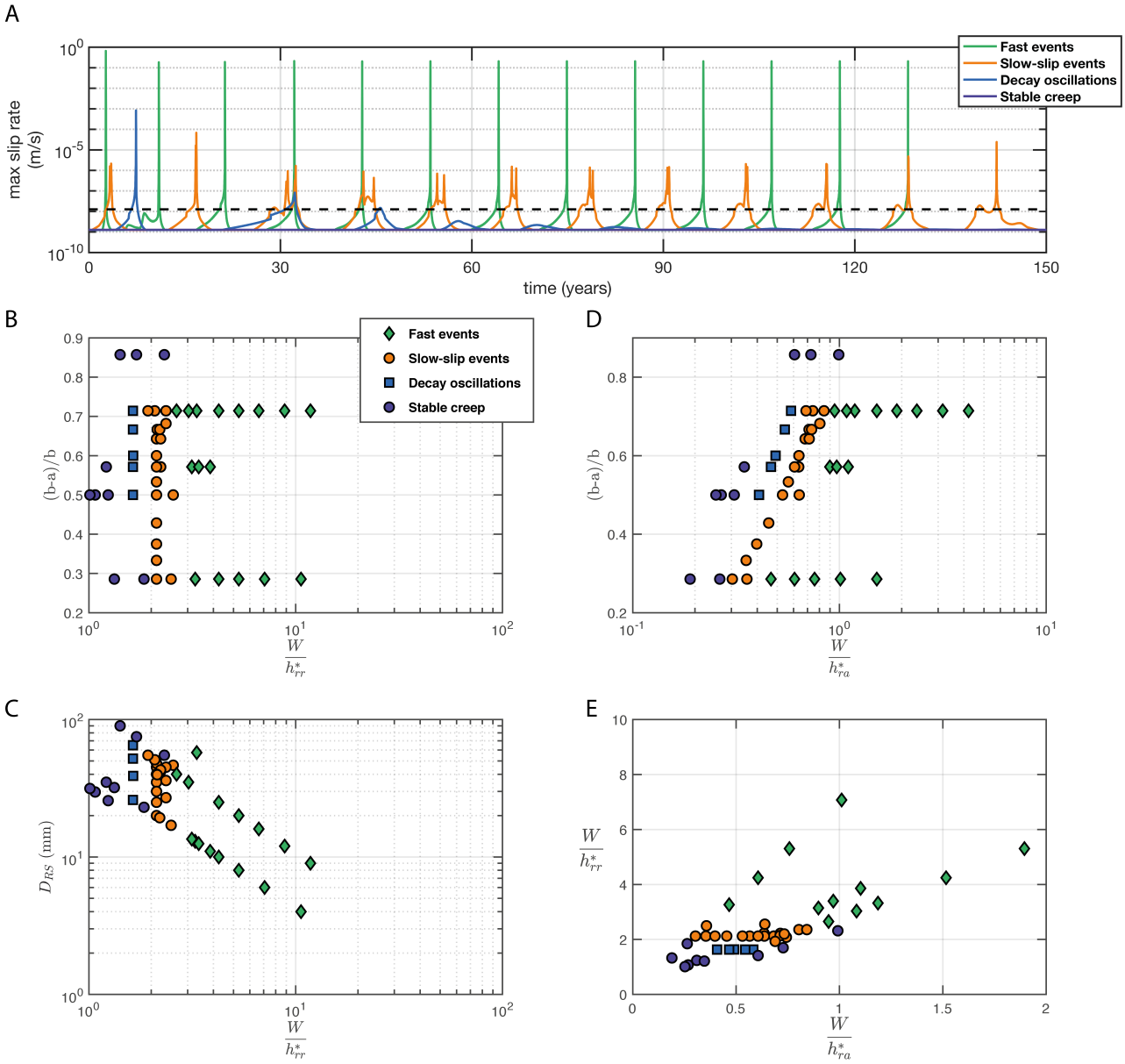


**Figure S1: The patterns of slip simulated in our model with rate-and-state friction and no dilatancy, for a range of rate-and-state properties (Table S1).** (**A**) Different slip patterns identified in our numerical models, based on model M1 and its variants. The model response changes from sequences of regular, fast, seismic earthquake ruptures, to sequences of slow-slip events, to decaying oscillations in slip rate, and to stable creep throughout the model. The black dashed line is the slip-velocity threshold used to determine the duration, along-strike length, area, rupture velocity, and magnitude of slow-slip events. (**B–E**) The dependence of model outcomes on frictional parameters. Slow slip events arise when the width $W$ of the velocity-weakening patch is in between two instability length scales, $h^*_{rr}$ and $h^*_{ra}$, with $W/3 < h^*_{rr} < W/2$.

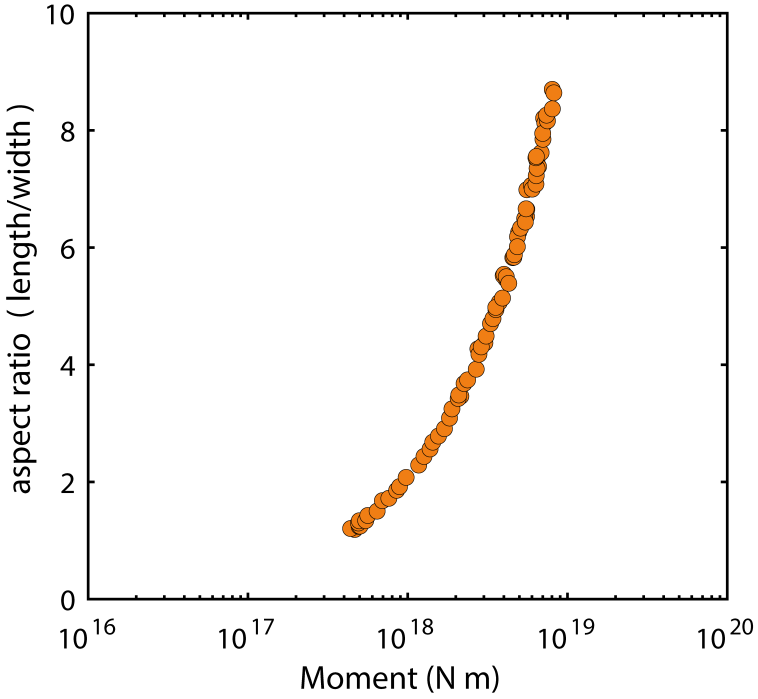


**Figure S2:** Aspect ratio of simulated slow-slip events from the reference model M1 (with dilatancy) shown in Fig. 2–4.

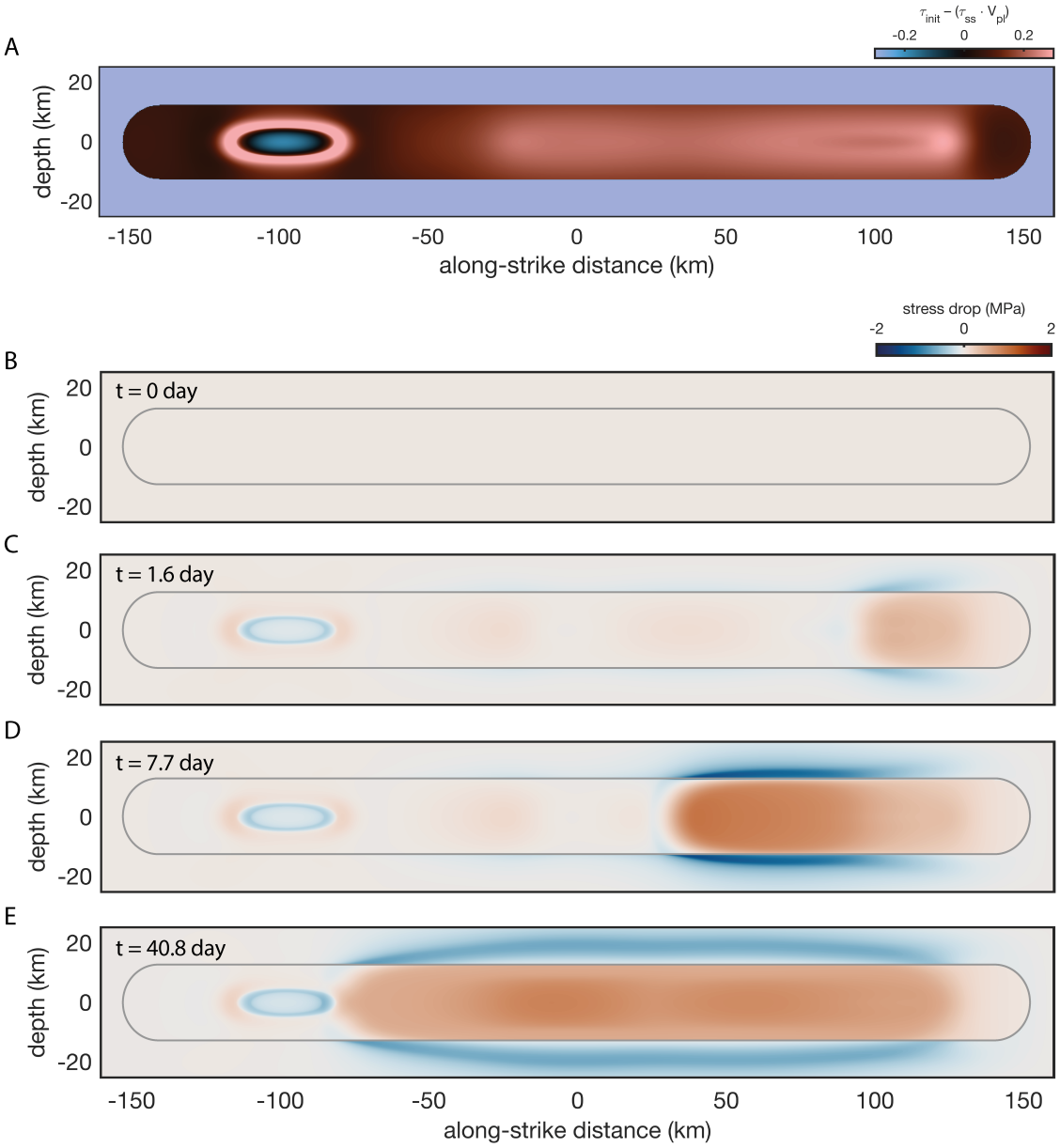


**Figure S3: Stress changes during the simulated SSE shown in Fig. 2.** (Top panel **A**) Shear stress state before the SSE, with the steady-state value of shear stress at the plate rate subtracted for clarity. (Bottom four panel **B–E**) Different stages of slow-slip propagation (the same as in Fig. 2) illustrated by snapshots of stress drop (blue-to-red colormap), with zero corresponding to the shear stress state before the event. Since the slip is slow and quasi-static, the along-strike propagation causes evolving quasi-static stress changes. Negative stress drop (i.e., stress increase) outside the rupture is absorbed and partially dissipated in the frictionally stable velocity-strengthening region, while positive stress drop occurs within the conditionally unstable velocity-weakening patch. The small patch of increasingly negative stress drop at the left corner of the fault is the result of a separate slip process, in which the small locked patch (Fig. 2) shrinks due to creep outside (with slip rates that are lower than the SSE threshold), with increasing stress over the patch. However, the stresses over the patch remain small and arrest the propagating SSE.

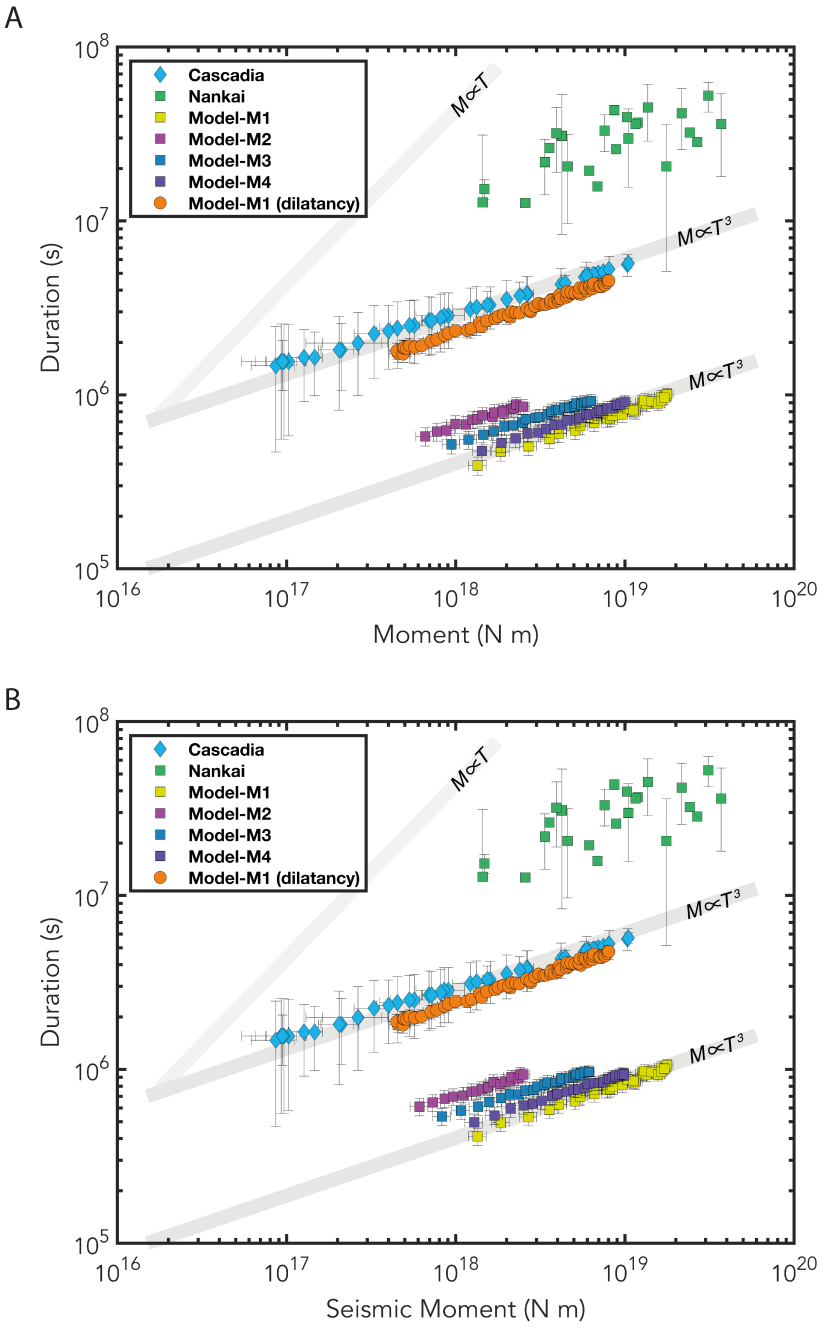


**Figure S4: Moment-duration scaling for the five models of Table S2 and its sensitivity to the choice of different thresholds in defining SSEs.** (**A**) Moment-duration scaling assuming a slip velocity threshold of $1.26 \times 10^{-8}$ m/s (i.e., 10 times faster than the long-term slip rate). (**B**) Moment-duration scaling assuming a slip velocity threshold of $2.53 \times 10^{-9}$ m/s (i.e., 2 times faster than the long-term slip rate) and a moment rate threshold of $10^{14}$ N m/day.

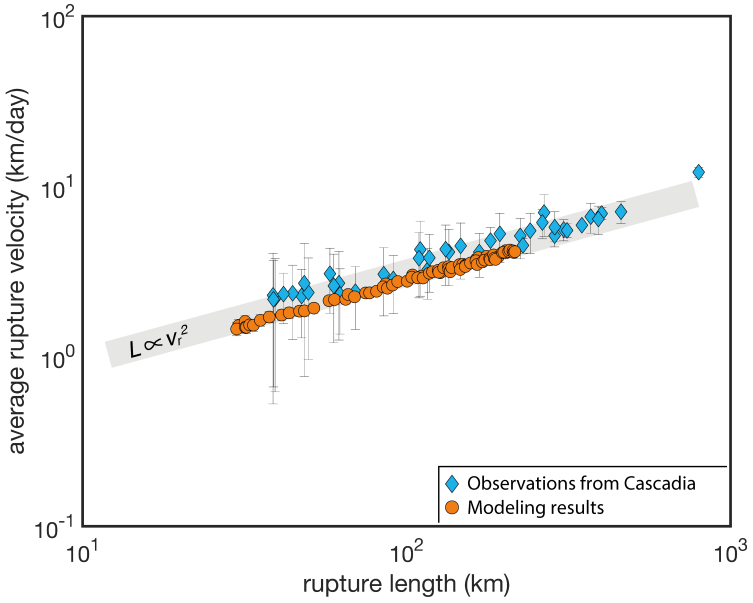


**Figure S5: Rupture length vs. average rupture velocity of slow-slip events from numerical experiments (orange dots) and observations from the Cascadia subduction zone (blue diamonds). Grey shading illustrates the scaling trend of $L \propto v_r^2$.**

**Movie S1: Long-term simulation of SSEs in a 3D fault model.** The movie illustrates the occurence of SSEs on the frictionally unstable (velocity-weakening) patch. The distribution of fault slip rates in color on a logarithmic scale, with the simulated time shown above the panel. The time steps are adaptive: smaller during SSEs and larger for post- and inter-event periods. During the inter-event period, creep penetrates into the rate-weakening patch. When a SSE nucleates, it expands in a semi-circular fashion until it saturates the width of the rate-weakening patch. Afterwards, it proceeds by propagating along strike.

**Supporting References**


Audet, P., Bostock, M. G., Christensen, N. I., & Peacock, S. M. (2009). Seismic evidence for overpressured subducted oceanic crust and megathrust fault sealing. *Nature*, *457*(7225), 76.

Barbot, S. (2019). Slow-slip, slow earthquakes, period-two cycles, full and partial ruptures, and deterministic chaos in a single asperity fault. *Tectonophysics*, *768*, 228171.

Bartlow, N. M., Miyazaki, S., Bradley, A. M., & Segall, P. (2011). Space-time correlation of slip and tremor during the 2009 cascadia slow slip event. *Geophysical Research Letters*, *38*(18).

Beeler, N., Tullis, T., Blanpied, M., & Weeks, J. (1996). Frictional behavior of large displacement experimental faults. *Journal of Geophysical Research: Solid Earth*, *101*(B4), 8697–8715.

Beeler, N., Tullis, T., & Goldsby, D. (2008). Constitutive relationships and physical basis of fault strength due to flash heating. *Journal of Geophysical Research: Solid Earth*, *113*(B1).

Bhattacharya, P., Rubin, A. M., & Beeler, N. M. (2017). Does fault strengthening in laboratory rock friction experiments really depend primarily upon time and not slip? *Journal of Geophysical Research: Solid Earth*, *122*(8), 6389–6430.

Chen, T., & Lapusta, N. (2009). Scaling of small repeating earthquakes explained by interaction of seismic and aseismic slip in a rate and state fault model. *Journal of Geophysical Research: Solid Earth*, *114*(B1).

Day, S. M., Dalguer, L. A., Lapusta, N., & Liu, Y. (2005). Comparison of finite difference and boundary integral solutions to three-dimensional spontaneous rupture. *Journal of Geophysical Research: Solid Earth*, *110*(B12).

Dieterich, J. H. (1979). Modeling of rock friction: 1. experimental results and constitutive equations. *Journal of Geophysical Research: Solid Earth*, *84*(B5), 2161–2168.

Dieterich, J. H., et al. (1981). Constitutive properties of faults with simulated gouge. *Mechanical Behavior of*.

Fu, Y., Liu, Z., & Freymueller, J. T. (2015). Spatiotemporal variations of the slow slip event between 2008 and 2013 in the southcentral alaska subduction zone. *Geochemistry, Geophysics, Geosystems*, *16*(7), 2450–2461.

Gao, X., & Wang, K. (2017). Rheological separation of the megathrust seismogenic zone and episodic tremor and slip. *Nature*, *543*(7645), 416.

Hawthorne, J., & Rubin, A. M. (2013). Laterally propagating slow slip events in a rate and state friction model with a velocity-weakening to velocity-strengthening transition. *Journal of Geophysical Research: Solid Earth*, *118*(7), 3785–3808.

Houston, H., Delbridge, B. G., Wech, A. G., & Creager, K. C. (2011). Rapid tremor reversals in cascadia generated by a weakened plate interface. *Nature Geoscience*, *4*(6), 404.

Ide, S., Beroza, G. C., Shelly, D. R., & Uchide, T. (2007). A scaling law for slow earthquakes. *Nature*, *447*(7140), 76.

Kato, A., & Nakagawa, S. (2014). Multiple slow-slip events during a foreshock sequence of the 2014 iquique, chile mw 8.1 earthquake. *Geophysical Research Letters*, *41*(15), 5420–5427.

Lapusta, N., & Liu, Y. (2009). Three-dimensional boundary integral modeling of spontaneous earthquake sequences and aseismic slip. *Journal of Geophysical Research: Solid Earth*, *114*(B9).

Lapusta, N., Rice, J. R., Ben-Zion, Y., & Zheng, G. (2000). Elastodynamic analysis for slow tectonic loading with spontaneous rupture episodes on faults with rate-and state-dependent friction. *Journal of Geophysical Research: Solid Earth*, *105*(B10), 23765–23789.

Leeman, J., Saffer, D., Scuderi, M., & Marone, C. (2016). Laboratory observations of slow earthquakes and the spectrum of tectonic fault slip modes. *Nature communications*, *7*, 11104.

Li, D., & Liu, Y. (2016). Spatiotemporal evolution of slow slip events in a nonplanar fault model for northern cascadia subduction zone. *Journal of Geophysical Research: Solid Earth*, *121*(9),

6828–6845.

Li, S., Freymueller, J., & McCaffrey, R. (2016). Slow slip events and time-dependent variations in locking beneath lower cook inlet of the alaska-aleutian subduction zone. *Journal of Geophysical Research: Solid Earth*, *121*(2), 1060–1079.

Liu, Y., & Rice, J. R. (2005). Aseismic slip transients emerge spontaneously in three-dimensional rate and state modeling of subduction earthquake sequences. *Journal of Geophysical Research: Solid Earth*, *110*(B8).

Liu, Y., & Rice, J. R. (2007). Spontaneous and triggered aseismic deformation transients in a subduction fault model. *Journal of Geophysical Research: Solid Earth*, *112*(B9).

Liu, Y., & Rubin, A. M. (2010). Role of fault gouge dilatancy on aseismic deformation transients. *Journal of Geophysical Research: Solid Earth*, *115*(B10).

Luo, Y., & Ampuero, J.-P. (2018). Stability of faults with heterogeneous friction properties and effective normal stress. *Tectonophysics*, *733*, 257–272.

Marone, C. (1998). Laboratory-derived friction laws and their application to seismic faulting. *Annual Review of Earth and Planetary Sciences*, *26*(1), 643–696.

Marone, C., Raleigh, C. B., & Scholz, C. (1990). Frictional behavior and constitutive modeling of simulated fault gouge. *Journal of Geophysical Research: Solid Earth*, *95*(B5), 7007–7025.

Matsuzawa, T., Hirose, H., Shibazaki, B., & Obara, K. (2010). Modeling short-and long-term slow slip events in the seismic cycles of large subduction earthquakes. *Journal of Geophysical Research: Solid Earth*, *115*(B12).

Michel, S., Gualandi, A., & Avouac, J.-P. (2018). Interseismic coupling and slow slip events on the cascadia megathrust. *Pure and Applied Geophysics*, 1–25.

Noda, H., & Lapusta, N. (2010). Three-dimensional earthquake sequence simulations with evolving temperature and pore pressure due to shear heating: Effect of heterogeneous hydraulic

diffusivity. *Journal of Geophysical Research: Solid Earth*, *115*(B12).

Noda, H., Lapusta, N., & Kanamori, H. (2013). Comparison of average stress drop measures for ruptures with heterogeneous stress change and implications for earthquake physics. *Geophysical Journal International*, *193*(3), 1691–1712.

Palmer, A. C., & Rice, J. R. (1973). The growth of slip surfaces in the progressive failure of over-consolidated clay. *Proceedings of the Royal Society of London. A. Mathematical and Physical Sciences*, *332*(1591), 527–548.

Rice, J. R., Lapusta, N., & Ranjith, K. (2001). Rate and state dependent friction and the stability of sliding between elastically deformable solids. *Journal of the Mechanics and Physics of Solids*, *49*(9), 1865–1898.

Rice, J. R., & Ruina, A. L. (1983). Stability of steady frictional slipping. *Journal of applied mechanics*, *50*(2), 343–349.

Rubin, A. M. (2008). Episodic slow slip events and rate-and-state friction. *Journal of Geophysical Research: Solid Earth*, *113*(B11).

Rubin, A. M., & Ampuero, J.-P. (2005). Earthquake nucleation on (aging) rate and state faults. *Journal of Geophysical Research: Solid Earth*, *110*(B11).

Ruina, A. (1983). Slip instability and state variable friction laws. *Journal of Geophysical Research: Solid Earth*, *88*(B12), 10359–10370.

Scholz, C. H. (1998). Earthquakes and friction laws. *Nature*, *391*(6662), 37–42.

Segall, P., & Rice, J. R. (1995). Dilatancy, compaction, and slip instability of a fluid-infiltrated fault. *Journal of Geophysical Research: Solid Earth*, *100*(B11), 22155–22171.

Segall, P., & Rice, J. R. (2006). Does shear heating of pore fluid contribute to earthquake nucleation? *Journal of Geophysical Research: Solid Earth*, *111*(B9).

Segall, P., Rubin, A. M., Bradley, A. M., & Rice, J. R. (2010). Dilatant strengthening as a

mechanism for slow slip events. *Journal of Geophysical Research: Solid Earth*, *115*(B12).

Shibazaki, B., & Iio, Y. (2003). On the physical mechanism of silent slip events along the deeper part of the seismogenic zone. *Geophysical Research Letters*, *30*(9).

Shibazaki, B., & Shimamoto, T. (2007). Modelling of short-interval silent slip events in deeper subduction interfaces considering the frictional properties at the unstable—stable transition regime. *Geophysical Journal International*, *171*(1), 191–205.

Suppe, J. (2014). Fluid overpressures and strength of the sedimentary upper crust. *Journal of Structural Geology*, *69*, 481–492.

Tsang, L. L., Meltzner, A. J., Philibosian, B., Hill, E. M., Freymueller, J. T., & Sieh, K. (2015). A 15 year slow-slip event on the sunda megathrust offshore sumatra. *Geophysical Research Letters*, *42*(16), 6630–6638.

Veedu, D. M., & Barbot, S. (2016). The parkfield tremors reveal slow and fast ruptures on the same asperity. *Nature*, *532*(7599), 361.

Viesca, R. C., & Dublanchet, P. (2018). The slow slip of viscous faults. *Journal of Geophysical Research: Solid Earth*.

Villegas-Lanza, J. C., Nocquet, J.-M., Rolandone, F., Vallée, M., Tavera, H., Bondoux, F., ... Chlieh, M. (2016). A mixed seismic–aseismic stress release episode in the andean subduction zone. *Nature Geoscience*, *9*(2), 150–154.

Wech, A. G., & Bartlow, N. M. (2014). Slip rate and tremor genesis in cascadia. *Geophysical Research Letters*, *41*(2), 392–398.

Ye, L., Lay, T., Kanamori, H., & Rivera, L. (2016). Rupture characteristics of major and great ($mw \geq 7.0$) megathrust earthquakes from 1990 to 2015: 1. source parameter scaling relationships. *Journal of Geophysical Research: Solid Earth*, *121*(2), 826–844.